

## Research Paper

# Forsteritic olivine and magnesium-rich orthopyroxene materials measured by Chang'e-4 rover

Sheng Gou<sup>a,b</sup>, Kaichang Di<sup>a,b,c</sup>, Zongyu Yue<sup>a,c,\*</sup>, Zhaoqin Liu<sup>a</sup>, Zhiping He<sup>d</sup>, Rui Xu<sup>d</sup>, Bin Liu<sup>a,b</sup>, Man Peng<sup>a</sup>, Wenhui Wan<sup>a</sup>, Yexin Wang<sup>a</sup>, Jianzhong Liu<sup>e</sup>

<sup>a</sup> State Key Laboratory of Remote Sensing Science, Aerospace Information Research Institute, Chinese Academy of Sciences, Beijing 100101, China

<sup>b</sup> State Key Laboratory of Lunar and Planetary Sciences, Macau University of Science and Technology, Macau, China

<sup>c</sup> CAS Center for Excellence in Comparative Planetology, Hefei 230026, China

<sup>d</sup> Key Laboratory of Space Active Opto-Electronics Technology, Shanghai Institute of Technical Physics, Chinese Academy of Sciences, Shanghai 200083, China

<sup>e</sup> Institute of Geochemistry, Chinese Academy of Sciences, Guiyang 550002, China



## ARTICLE INFO

## Keywords:

Chang'e-4 rover  
In situ spectral measurements  
Finsen crater ejecta  
Differentiated impact melt pool  
Mg-suite pluton

## ABSTRACT

China's Chang'e-4 probe achieved the first soft landing within the South Pole-Aitken (SPA) basin, which is the oldest, largest, and deepest basin on the lunar farside. The deployed Chang'e-4 rover made in situ spectral measurements along the rover traverse during a nominal three-month mission period. Spectral analyses imply that materials at the Chang'e-4 landing site have a forsteritic olivine (OL) and magnesium (Mg)-rich orthopyroxene (OPX) assemblage in almost equal fractions. The Chang'e-4 rover measured materials, which were essentially mixture of multiple sources, were primarily the weathering products of Finsen crater ejecta. Plagioclase (PLG), which has significant implication for the provenance, is often spectrally transparent or featureless in the wavelength range (450–2395 nm) of the in situ measured spectrum. Depending on the possible absence or presence of abundant PLG, the materials likely originated from a differentiated SPA impact melt pool or from an Mg-suite pluton in the lunar lower crust, and were less likely to originate from the lunar upper mantle.

## 1. Introduction

The South Pole-Aitken (SPA) basin is recognized as the largest, deepest, and oldest impact basin on the Moon (Stuart-Alexander, 1978; Wilhelms et al., 1979; Spudis et al., 1994). Although studies have suggested the SPA-forming impact was perhaps very oblique, and thus maybe have excavated only shallowly into the lunar crust (Garrick-Bethell and Zuber, 2009; Schultz and Crawford, 2011), recent simulation works revealed that the basin-forming impact should have penetrated the lunar crust and exposed the lunar mantle materials (Miljkovic et al., 2015; Melosh et al., 2017; Zhu et al., 2018). Because it provides both a unique window to study the structure and constitution of the lunar interior (Ennis et al., 2012) and a portal to the early history of the solar system, especially relating to postaccretionary heavy bombardment (Jolliff et al., 2010), exploring the SPA basin ranks as a high priority for lunar and solar system science by the National Research Council (NRC, 2011).

China's Chang'e-4 probe successfully landed in the Von Kármán crater inside the SPA basin on January 3, 2019, making the first soft

landing of a probe on the lunar farside (Wu et al., 2019). A lunar rover equipped with several scientific payloads was deployed on the same day. The Chang'e-4 rover conducted a series of in situ measurements along its traverse. Interpretations of the measured datasets provide first-hand information on the geomorphology, mineral composition, and subsurface structure within the Von Kármán crater and could shed light on the understanding of the lunar evolution. This study analyzes the in situ measured spectra on lunar surface materials during the nominal three-month mission period. Mineral compositions and relative fractions of the measured materials are inferred from spectral deconvolution outputs.

## 2. Instrument and measurement

## 2.1. Specifications of the instrument

Three payloads are installed on the Chang'e-4 rover: a panoramic camera, a lunar-penetrating radar, and a Visible and Near-Infrared Imaging Spectrometer (VNIS) (Wu et al., 2019). This study focuses on

\* Corresponding author at: P. O. Box 9718, Datun Road, Chaoyang District, Beijing 100101, China.

E-mail address: [yuezy@radi.ac.cn](mailto:yuezy@radi.ac.cn) (Z. Yue).

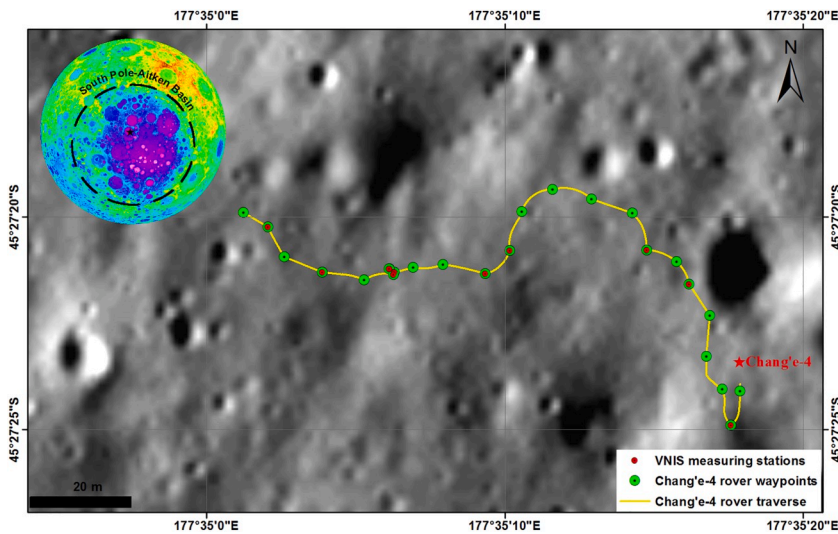


**Fig. 1.** Traverse map of the Chang'e-4 rover during the first 3 lunar days. The base map is a high resolution (0.9 m/pixel) digital orthophoto map (DOM) (Liu et al., 2019) generated from Lunar Reconnaissance Orbiter Camera (LROC) Narrow Angle Camera (NAC) imagery (Robinson et al., 2010). The Lunar Orbiter Laser Altimeter (LOLA) elevation (Smith et al., 2010) inset shows Chang'e-4 landing site within the SPA basin (black star). Colors represent different heights in the inset, with red being the highest and purple being the lowest.

spectral datasets measured by the VNIS. The VNIS is mainly composed of a visible/near-infrared (VIS/NIR) imaging spectrometer, a shortwave infrared (SWIR) spectrometer, and a white panel for calibration and dust-proofing (He et al., 2019; Li et al., 2019). The spectral range is 450–2395 nm with a default sampling interval of 5 nm, and the total number of spectral channels is 400 (with 10 overlapping channels between 900 and 945 nm) (He et al., 2019; Li et al., 2019). The effective image sizes of the VIS/NIR imaging spectrometer are  $256 \times 256$  pixels, and the spatial resolution is approximately 1 mm/pixel from a typical 1 m detection distance. The field of view (FOV) of the SWIR spectrometer corresponds to a circular region in the VIS/NIR image with the center located at (96, 128) and a radius of 54 pixels (He et al., 2019; Li et al., 2019).

## 2.2. In situ spectral measurements

Since the successful deployment on the lunar surface, the Chang'e-4 rover traversed about 163 m during its nominal three-month mission period. The VNIS made 13 measurements on lunar regolith and 1 measurement on an about 20-cm rock fragment along the rover traverse (Fig. 1 and Supplementary Table 1).

## 3. Methods

### 3.1. Full-spectrum reflectance derivation

The spectral analysis is based on the Level 2B (L2B) radiance

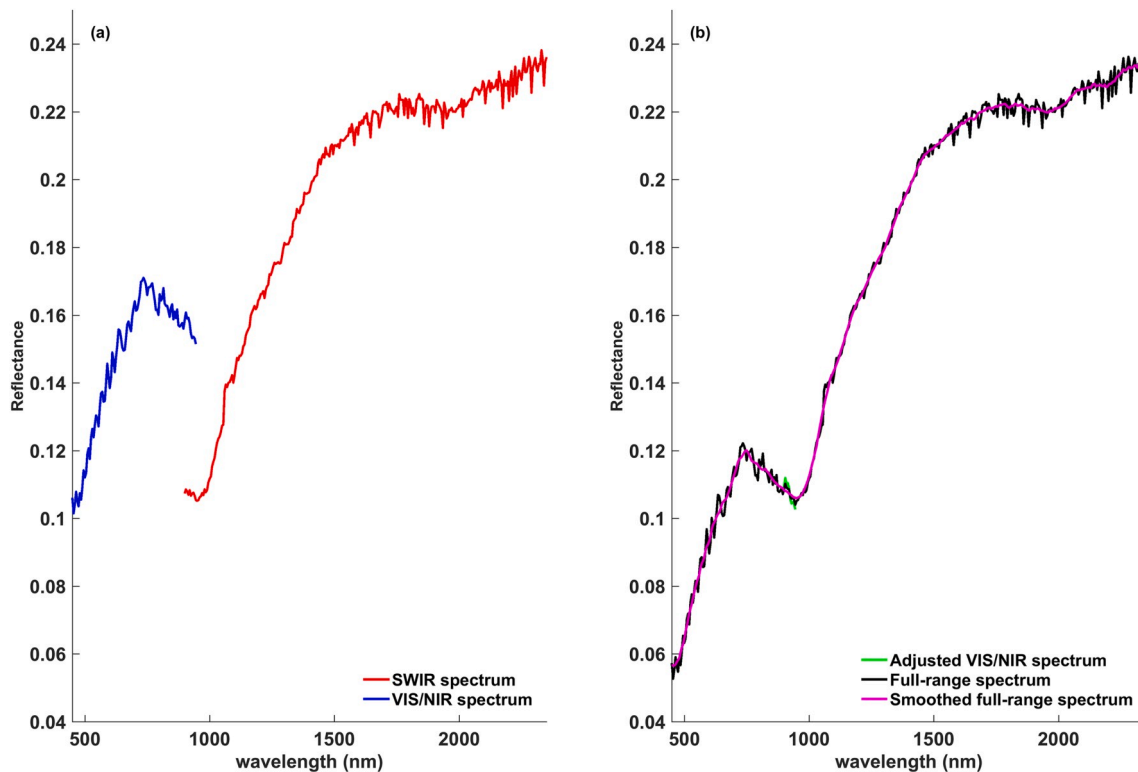


**Fig. 2.** Spectrum measured at rover station LE00303 for a rock fragment. (a) Illustration of spectrum discontinuity; (b) Illustration of eliminating discontinuity and smoothing spectrum.

datasets, which are produced and released online by the Ground Research and Application System (GRAS). The L2B radiance datasets are first corrected by onboard radiometric calibration coefficients for both the VIS/NIR and SWIR spectrometers. These calibration coefficients are obtained from the onboard synchronous calibration experiments that were performed during the three lunar days and are provided by the VNIS manufacturer. The reflectance (reflectance factor, REFF) is then derived in this study by the solar irradiance calibration method (Wu et al., 2018).

A gap exists at the overlapping bands of the VIS/NIR and SWIR spectra (Fig. 2a). Because the SWIR spectrum has a higher signal-to-noise ratio and stability than the average VIS/NIR spectrum (He et al., 2019; Li et al., 2019), the VIS/NIR spectrum in the FOV of the SWIR spectrometer is adjusted to the SWIR spectrum by moving the VIS/NIR spectrum around with an offset (Fig. 2b). The offset is the difference between the average reflectance of the overlapping bands from 900 to 945 nm. The full-range spectrum from 450 to 2395 nm is thus constructed and it is smoothed by a simple 11-points moving average method (Fig. 2b). Continuum is removed during spectral deconvolution by the following described Modified Gaussian model (MGM). The process removes the overall curvature of the spectrum, and normalizes it so that individual absorption feature of interest is compared from a common baseline. Therefore, the influence of moving the spectrum around to derive full-range spectrum has minor influence on making relative, qualitative assessments of general mineralogical trends in this study.

### 3.2. Mineral composition identification

The primary rock-forming minerals on the lunar surface are pyroxene (PYX), olivine (OL), and plagioclase (PLG). PYX is roughly classified as orthopyroxene (OPX) and clinopyroxene (CPX) based on chemistry and crystallography (Burns, 1993). PLG dominates the lunar highlands, while OPX, CPX, and OL dominate the mare regions (Pieters, 1986; Spudis and Davis, 1986). These minerals can be uniquely distinguished by their specific spectral characteristics in the wavelength range of the Chang'e-4 rover measured spectrum. Both OPX and CPX spectra exhibit Gaussian shape absorption features. Their absorption positions shift with the content of Fe/Ca/Mg. OPX has absorptions at ~900 nm and ~1900 nm, respectively. CPX has absorptions at ~1000 nm and ~2200 nm, respectively (Adams, 1974; Denevi et al., 2007). Typical pure OL spectrum has three overlapping absorption features at approximately 850, 1050, and 1250 nm, forming what appears to be a single, broad, and composite absorption feature near 1050 nm (Burns, 1970; Sunshine and Pieters, 1998). The overall absorption center shifts towards longer wavelengths with increasing Fe (Burns, 1970), and the absorption band of fayalite (Fe-rich OL) is broader and more flat-bottomed than that of forsterite (Mg-rich OL) (Sunshine and Pieters, 1998). PLG is often considered as a spectrally transparent or featureless mineral. On one hand, due to incorporation of minor amounts of FeO (<1.0 wt%), iron-bearing crystalline PLG spectrum has only one weak and broad absorption near 1250 nm (Adams and Goullaud, 1978; Burns, 1993). However, this feature is easily masked by a few to several vol% of mafic minerals in a mixture. Cheek and Pieters (2014) showed that as little as 2 vol% of OL or PYX completely masks the PLG signal. On the other hand, due to shock-induced loss of crystal structure, many lunar PLGs are spectrally featureless (Adams et al., 1979; Bruckenthal and Pieters, 1984). Therefore, PLG cannot be assessed with Chang'e-4 rover measured spectral datasets alone. Nevertheless, the possible presence or absence of abundant PLG in the Chang'e-4 rover measured materials, which has important implications, is discussed in this study.

In addition, other components in the regolith, such as opaque minerals (e.g., ilmenite), and maturation products (e.g., agglutinitic glass), also contribute to the overall reflectance and have significant implications. Ilmenite is highly absorbing and strongly affects the reflectance spectrum when its abundance is high (e.g., ilmenite-rich (>17%) Apollo 17 bulk rock samples), especially for the fine particle size samples

(Moriarty and Pieters, 2016). Compared with the ilmenite-rich Apollo 17 samples, TiO<sub>2</sub> abundance at Chang'e-4 landing site estimated from Selenological and Engineering Explorer (SELENE) multiband imager (MI) data is about  $1.42 \pm 0.24$  wt% (Otake et al., 2012) (Supplementary Fig. 1), thus the ilmenite does not strongly affect the overall continuum compared with PYX and OL. Iron-bearing glass (GLS) spectrum exhibits two broad and symmetric absorptions typically centered between 1070 and 1200 nm, and between 1090 and 2050 nm (Horgan et al., 2014). However, the 1000 nm broad iron band absorption of GLS is easily suppressed by iron-bearing mafic minerals and nanophase iron that are ubiquitous in the lunar regolith (Cannon and Mustard, 2015). Therefore, possible presence of these components is not discussed here either.

### 3.3. MGM deconvolution and composition prediction

Modified Gaussian model (MGM), originally proposed by Sunshine et al. (1990) and revised by Clénet et al. (2011), is an analytical tool to deconvolve overlapping absorptions of mafic mineral spectrum into their fundamental absorption components (Sunshine et al., 1990). One Gaussian function (characterized by band center, width and strength) or combination of multiple Gaussian functions permits the identification of a mineralogical absorption band, indicative of the presence and composition of the predominant mafic minerals (Sunshine and Pieters, 1998). MGM is used in this study with 7 different configurations (Supplementary Table 2) to deconvolve overlapping absorptions of each VNIS measured spectrum into their fundamental absorptions. For example, The 'OL-OPX' configuration (Supplementary Table 2) has 6 Gaussians, including 1 for strong absorption centered around 450 nm in ultraviolet (UV) region (UV450), 3 for OL absorptions (OL850, OL1050, and OL1250), and 2 for OPX absorptions (OPX900 and OPX1900) (Clénet et al., 2011). The spectrum continuum is fitted by a second order polynomial with anchoring points adjusted on the local maxima along the spectrum and initial parameters of each Gaussian are made on the basis of laboratory results (Clénet et al., 2011). As one spectrum may be fitted with multiple candidate configurations, the fitting with the least root mean square error (RMSE) is selected as the optimum among candidate configurations that have physical meaning (i.e., satisfy the spectroscopic criteria).

MGM outputs are informative of the chemical composition of OL and PYX (Sunshine and Pieters, 1998; Kanner et al., 2007). To predict the Mg number (Fo#) of a given spectrum that is modeled with OL-related configurations, the MGM modeled three OL-related band centers are fitted to a laboratory derived compositional trend line by finding the least error (Sunshine and Pieters, 1998; Isaacson and Pieters, 2010). It should be noted here that the uncertainty of predicted Fo# arises from slight variations in initial spectral parameters and other errors (e.g., spectrum with lower signal-to-noise ratio) is likely to be on the order of 5–10% Fo# range (Isaacson and Pieters, 2010; Pinet et al., 2018; Pinet et al., 2019). Kanner et al. (2007) assessed relationship between normalized band strength ratio (NBSR) that calculated from MGM derived band depths (also called absorption strengths) and the known mineral fractions in an OPX and CPX mixture. The estimated OPX and CPX fraction errors are constrained to  $\pm 10\%$ , which is still robust in the presence of up to 10–15% OL (Kanner et al., 2007). The concept of NBSR including OL has been subsequently introduced by Clénet et al. (2011). MGM is able to model simple and complex mafic mineralogies, including binary and ternary OL–PYX mixtures, for a large range of grain sizes (Clénet et al., 2011). Five NBSR values (if applicable) are calculated in this study to estimate relative mineral fractions (Table 1).

## 4. Results

### 4.1. Spectroscopic features of lunar surface materials

According to space weathering studies (Pieters and Noble, 2016), the reflectance spectra measured by the Chang'e-4 rover should have

**Table 1**  
Formulae of normalized band strength ratio (NBSR).

NBSR	Definition	
1000 nm absorption feature	NBSR(OL)	$\frac{BD1000(OL)^*}{BD1000(OL) + BD1000(OPX) + BD1000(CPX)}$
	NBSR(OPX)	$\frac{BD1000(OPX)}{BD1000(OL) + BD1000(OPX) + BD1000(CPX)}$
	NBSR(CPX)	$\frac{BD1000(CPX)}{BD1000(OL) + BD1000(OPX) + BD1000(CPX)}$
		$\frac{BD1000(OL) + BD1000(OPX) + BD1000(CPX)}{BD1000(OL) + BD1000(OPX) + BD1000(CPX)}$
2000 nm absorption feature	NBSR(OPX)	$\frac{BD2000(OPX)}{BD2000(OPX) + BD2000(CPX)}$
	NBSR(CPX)	$\frac{BD2000(CPX)}{BD2000(OPX) + BD2000(CPX)}$
		$\frac{BD2000(OPX) + BD2000(CPX)}{BD2000(OPX) + BD2000(CPX)}$
		$\frac{BD2000(OPX) + BD2000(CPX)}{BD2000(OPX) + BD2000(CPX)}$

\*BD1000 and BD2000 are MGM derived band depths (also called absorption strengths) for OL, OPX, and CPX.

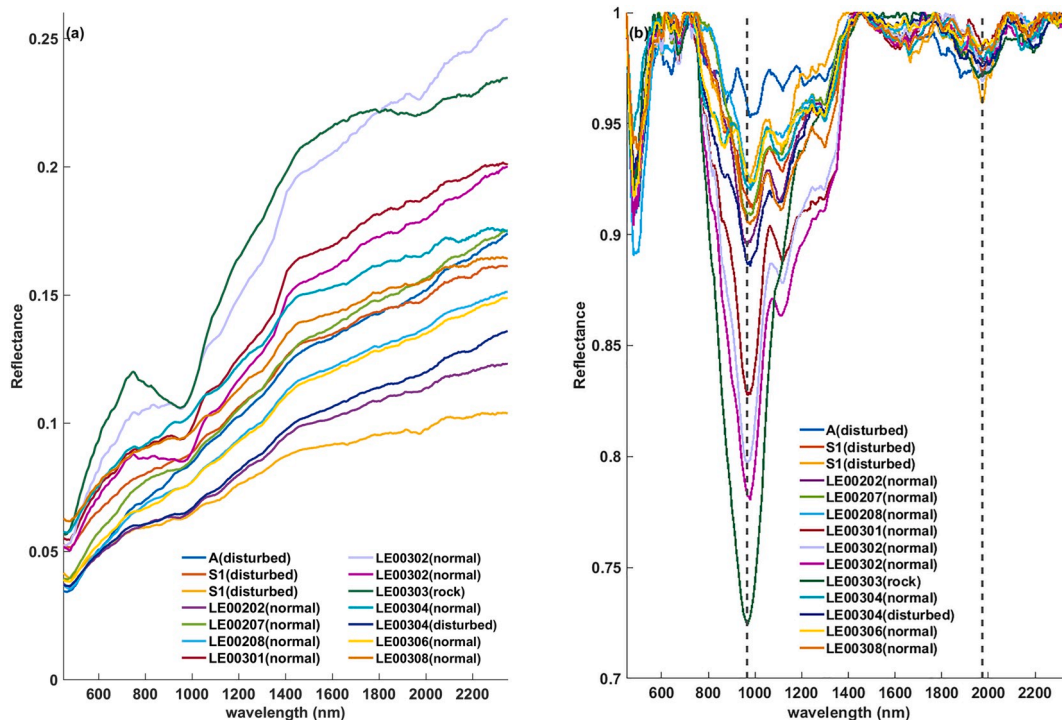


**Fig. 3.** Spectra measured by the Chang'e-4 rover at 11 different stations during the first three lunar days: (a) the original reflectance and (b) the continuum-removed spectrum. The dashed lines are located at 965 nm and 1975 nm. The discontinuity in some spectra in this figure near 1400 nm is related to signals that arise from artifacts of the instrument design.

**Table 2**  
MGM derived band centers, NBSR, and Fo# values.

Rover station (regolith state)	OL850 (nm)	OPX900 (nm)	OL1050 (nm)	OL1250 (nm)	OPX1900 (nm)	1000 nm absorption		Fo#
						NBSR(OL)	NBSR(OPX)	
S1 (disturbed)	840.3	940	1066.7	1182.6	1866.6	0.5	0.5	96
S1 (disturbed)	849.8	918.9	1107.5	1213.3	1837.4	0.6	0.4	65
LE00202 (normal)	845.9	954.5	1110.1	1194.1	1833.3	0.5	0.5	76
LE00301 (normal)	834.5	969.8	1070.9	1188	1848.1	0.5	0.5	94
LE00302 (normal)	850.1	967	1074.5	1182.7	1915.2	0.5	0.5	89
LE00302 (normal)	839.5	962.6	1071.7	1187.8	1910.4	0.6	0.4	92
LE00304 (normal)	844.4	906.5	1088	1179.7	1824.6	0.5	0.5	90
LE00304 (disturbed)	850	918.9	1078.5	1197.8	1908.2	0.5	0.5	80
LE00306 (normal)	850	900.4	1053	1183.7	1868.6	0.5	0.5	94
LE00308 (normal)	832.8	959.8	1087.3	1180.9	1816.2	0.5	0.5	95
Mean	843.7	939.8	1080.8	1189.1	1862.9	0.5	0.5	87
Standard deviation	6.6	26.5	17.8	10.3	37.2	0.0	0.0	10

Note that NBSR values represent relative mineral fractions, and the uncertainties are constrained to  $\pm 10\%$ .

suffered from space weathering. The in situ measured reflectance spectra exhibit typical features of an increasing spectral slope towards longer wavelengths (reddening), a darkening of the overall reflectance and a weakening of the absorption features (Fig. 3a). Two absorption features at approximately 1000 nm and 2000 nm are discernible from the continuum-removed spectra (Fig. 3b). The band depths of the 1000 nm absorption for PYX- and OL-bearing minerals are relatively stronger than that of the 2000 nm absorption for PYX.

#### 4.2. Mineral compositions of lunar regolith

The MGM fitting results show that 10 out of the 13 lunar regolith spectra can be optimally fitted with the 'OL-OPX' configuration (Supplementary Figs. 2 to 11), indicating that the Chang'e-4 rover measured regolith has an OL and OPX assemblage. The modeled OPX-related 1000 nm absorption centers vary from 900.4 nm to 969.8 nm ( $939.8 \pm 26.5$  nm) (Table 2), and the 2000 nm absorption centers vary from 1816.2 nm

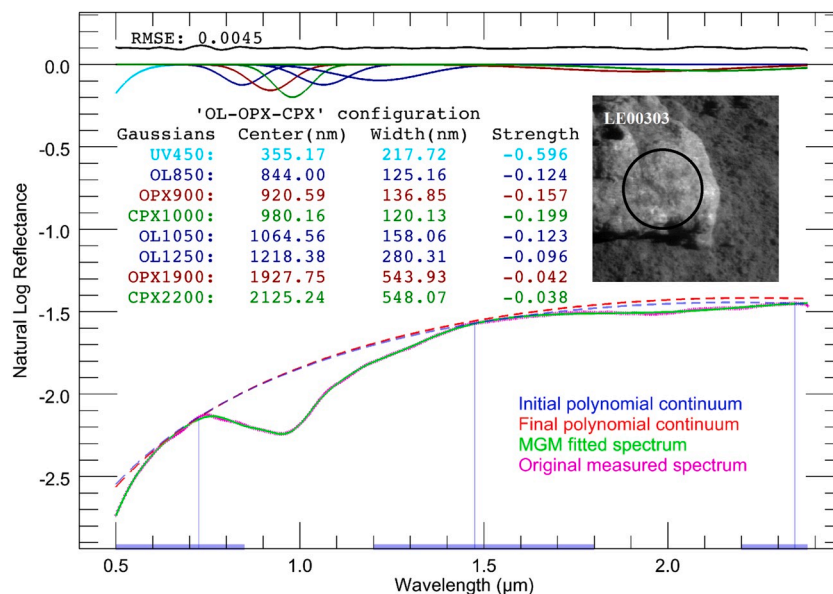


Fig. 4. Rock spectrum modeled with 'OL-OPX-CPX' configuration. The VIS/NIR image inset is taken at station LE00303 (the circle corresponds to the FOV of SWIR spectrometer).

**Table 3**  
NBSR values of the rock spectrum.

NBSR	1000 nm absorption			2000 nm absorption	
	NBSR(OL)	NBSR(OPX)	NBSR(CPX)	NBSR(OPX)	NBSR(CPX)
Value	0.2	0.4	0.4	0.5	0.5

Note: The NBSR values represent relative mineral fractions.

to 1915.2 nm ( $1862.9 \pm 37.2$  nm). The relative short band centers indicate that PYX in the regolith at the Chang'e-4 landing site is chiefly Mg-rich orthopyroxene (OPX). NBSR values (OL: OPX is 50%: 50%) (Table 2) indicate that OL and OPX are present in almost equal fractions in the regolith. The predicted magnesium number (Fo#  $87 \pm 10$ ) (Table 2), with an uncertainty on the order of 10, indicates that the OL is forsteritic (Mg-rich) OL. It should be noted here that the complex OL absorption feature not only varies with the iron content but also with grain size and abundance. As demonstrated by Clénet et al. (2011), a forsterite with very large grains and a fayalite with smaller grains may have similar spectral features. Thus high Fo# value is very tentative here and should be treated with caution for geological interpretation.

#### 4.3. Mineral composition of a rock fragment

MGM with the 'OL-OPX-CPX' configuration provides the best modeling results in terms of mineral detection for the rock spectrum (Fig. 4), and the modeled OL band centers predict that the Mg-number (Fo#) is 79, pointing at a Mg-rich composition. The short OPX absorption bands (920.6 nm and 1927.8 nm) indicate it is Mg-rich. NBSR values (Table 3) for the 1000-nm absorption feature predict that the relative fractions of OPX and CPX are equal (OL: OPX: CPX is 20%: 40%: 40%). NBSR values for the 2000-nm absorption features also predict that OPX and CPX are present in equal fractions (OPX: CPX is 50%: 50%), indicating self-consistency in the mineral fractions. The OL and OPX compositions of the rock fragment predicted from MGM fitting results are in agreement with that of the regolith, indicating that the rock fragment has a high probability of having the same source as the surrounding lunar regolith. Because of minerals' overlapping spectral absorption features and above stated grain size effects, it's also should be noted here further MGM modeling experiments should be carried out in well-constrained conditions to better understand the influence of the

presence of possible other components (e.g., PLG) and mineral grain sizes on assessing mineral compositions and estimating relative fractions (Pinet, 2019).

## 5. Discussion

### 5.1. Primary source of the in situ spectrally measured materials

The materials measured by Chang'e-4 rover were essentially mixtures of many origins, especially in a complex, ancient terrane such as the SPA basin. Obvious NE-SW trending linear features, which radiate from the ~73-km diameter Finsen crater (Fig. 5b), are observed from the elevation map of Chang'e-4 landing area (Huang et al., 2018). In addition, the MI reflectance mosaic (Supplementary Fig. 12) and false color composite (Supplementary Fig. 13) show that Chang'e-4 landed on a low-albedo region that was covered by old mixed/gardened ejecta materials. Compared with surrounding highest terrain in the Chang'e-4 landing area, topographic profiles, which are extracted from both an improved lunar digital elevation model (DEM) SLDEM2015 (512 pixels/degree) (Barker et al., 2016) and a Lunar Reconnaissance Orbiter Camera (LROC) Narrow Angle Camera (NAC)-derived Digital Terrain Model (DTM, about 5 m/pixel) ([http://wms.lroc.asu.edu/lroc/view\\_rdr/NAC\\_DTM\\_CHANGE4](http://wms.lroc.asu.edu/lroc/view_rdr/NAC_DTM_CHANGE4)), show that the Chang'e-4 probe just landed at the local highest terrain (Fig. 5c). Elevated terrains with intervals, which are interpreted as Finsen crater ejecta rays, are observed from both profiles. Ling et al. (2018) divided the mare region within the Von Kármán crater into two units: A low-Ti unit (LT,  $3 \text{ wt}\% > \text{TiO}_2 > 1.5 \text{ wt}\%$ ) and a Finsen ejecta unit (FE,  $\text{TiO}_2 < 1.5 \text{ wt}\%$ ). MI-derived  $\text{TiO}_2$  abundance within 5 km of landing site is  $1.42 \pm 0.24 \text{ wt}\%$  (Otake et al., 2012) (Supplementary Fig. 13), indicating Chang'e-4 probe landed on the FE unit. The elevation difference between the surrounding highest terrain (about -5915 m in the SLDEM2015) and the Chang'e-4 landing site (about -5925 m in the LROC NAC-derived DEM and about -5930 m in the SLDEM2015) probably reflects the thickness of the Finsen crater ejecta is uneven. Chang'e-4 probe just landed in a place where the ejecta thickness of the ejecta is relatively thin. On the basis of these analyses, it is proposed that the local mare basalt deposits at the Chang'e-4 landing site were extensively covered by ejecta from Finsen crater. And the Chang'e-4 rover measured forsteritic OL and Mg-rich OPX materials are primarily lunar deep-seated materials excavated from Finsen crater.

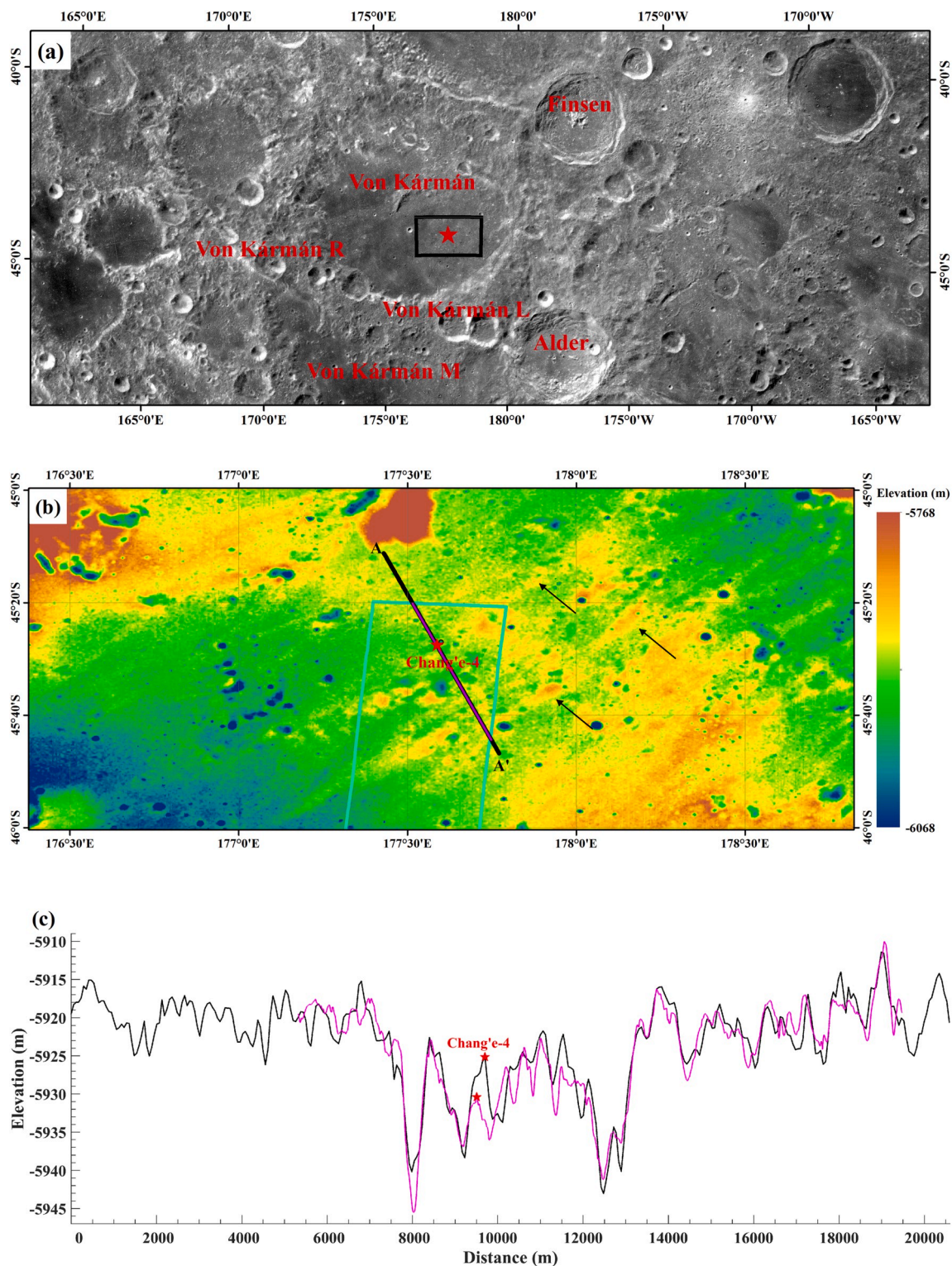


**Fig. 5.** (a). Chang'e-4 probe landing site (red star) inside the Von Kármán crater and surrounding craters within the SPA basin. The black rectangle marks the extent of the elevation map shown in b. (b). SLDEM2015 elevation map in the Chang'e-4 probe landing area. Black arrows indicate the NE-SW trend features. The cyan polygon is the footprint of LROC NAC-derived DTM. (c). Topographic profiles of A-A' that cross the Chang'e-4 probe landing site. Elevation data of black profile are extracted from SLDEM2015 and the magenta are from LROC NAC-derived DTM. The offset between the two stars that mark the Chang'e-4 probe landing site along the x-axis is caused by the two elevation datasets are not strictly co-registered. The offset along the y-axis is caused by the elevation accuracy of the two datasets.

### 5.2. Constrain for the provenance of the materials

Topographic and geologic context analysis reveals that the Chang'e-4 rover measured materials was primarily ejecta from Finsen crater.

MGM deconvolution of the in situ measured spectra implies that the materials at the landing site have a forsteritic OL and Mg-rich OPX assemblage in almost equal fractions. It cannot be ruled out the possibility that PLG is present, which has significant implication for the

provenance of the Chang'e-4 rover measured materials. However, PLG is often spectrally transparent due to mix with other mafic minerals or featureless due to shock-induced loss of crystal structure in the wavelength range (450–2395 nm) of the in situ measured spectrum. Depending on the possible absence or presence of a large amount of PLG, the Chang'e-4 rover measured materials may originate from: (1) lunar upper mantle; (2) differentiated SPA impact melt pool; (3) Mg-suite pluton in the lunar lower crust.

### 5.2.1. Lunar upper mantle scenario

Mantle materials are expected to be exposed by the basin-forming events (Miljkovic et al., 2015). The SPA basin-forming impact should have sampled the lunar lower crust and upper mantle even if it's a very oblique impact (e.g., impact at an angle of 20°) (Melosh et al., 2017; Zhu et al., 2018). The popular lunar magma ocean (LMO) hypothesis indicates that the lunar upper mantle is made mostly of OL and PYX (e.g., peridotite and dunite) due to cumulate overturn (Ringwood and Kesson, 1976), with Mg-rich OLs being believed to be the most abundant constituent (Fo is expected to be >90) under the assumption that all planets usually are like the Earth (Gaul et al., 2000). OL has indeed been remotely detected on several large-impact basin rims on the lunar surface, where the crust was substantially thinned through excavation (Yamamoto et al., 2010; Isaacson et al., 2011). However, the almost complete absence of evidence (e.g., dunite clasts) in the returned lunar samples (Shearer et al., 2015) challenges the hypothesis. Recent remote sensing observations and numeric simulations also challenge the current paradigm and argued that the upper mantle is dominated by OPX (Melosh et al., 2017). Therefore, the Chang'e-4 rover measured materials (Fo# 87 ± 10) may originate from the lunar mantle is a less likely scenario.

### 5.2.2. Differentiated melt pool scenario

The SPA basin-forming event should have sampled the lunar lower crust and upper mantle (Miljkovic et al., 2015; Melosh et al., 2017). A large portion as much as 60% ~ 80% of the impact-generated melts was retained within the SPA basin, forming a melt pool. The melt pool likely differentiated and formed a noritic layer with a thickness of ~6 km and possibly as thick as ~13 km (Hurwitz and Kring, 2014; Vaughan and Head, 2014). The estimated transient cavity radius of the SPA basin ranges from 840 km to 1400 km (Wieczorek and Phillips, 1999; Petro and Pieters, 2002; Potter et al., 2012). Finsen crater is just about 370 km from the center of the SPA basin. Therefore, the materials measured by Chang'e-4 rover were probably primarily the weathering products of the noritic rocks that mainly excavated from Finsen crater 3.61 billion years ago (Ivanov et al., 2018).

### 5.2.3. Mg-suite pluton scenario

OL that is present in mare basalt is usually Fe-rich (Papike et al., 1976), while a Mg-rich composition suggests a relatively primitive plutonic source (Isaacson et al., 2011). Despite the relative high Fo value, Apollo samples rich in OL have been confirmed to not necessarily contain mantle components. For example, OLs in Type C basalt 74,275 have forsterite contents ranging from 68.2–83.2, and 72,415 contains OL with forsterite contents >88 (Shearer et al., 2015). In addition, the definitive identification of SPA derived impact melt on the basin floor, either by remote sensing or via photogeology, is extremely difficult due to the number of subsequent impacts and volcanic activities (Petro, 2011). And the Finsen crater is on the margin of the proposed impact melt pool. Therefore, the possibility that the Chang'e-4 rover measured forsteritic OL and Mg-rich OPX materials may originate from an Mg-suite pluton in the lunar lower crust cannot be excluded in this study.

Based on these analyses, the Chang'e-4 rover measured forsteritic OL and Mg-rich OPX materials likely originated from the differentiated SPA impact melt pool or from an Mg-suite pluton in the lunar lower crust, and are less likely to originate from the lunar mantle. As SPA basin has not been sampled either by previous lunar sample return missions

(Apollo, Luna) or by lunar meteorites, a definitive answer to the sources of VNIS measured materials can only be addressed in the future through detailed analysis on returned samples. Specifically, trace element geochemistry or the amount and composition of minor minerals (including plagioclase) are needed to fully constrain the petrologic history of these materials.

## 6. Conclusion

Chang'e-4 rover made in situ spectral measurements during a nominal three-month mission period within the SPA basin on the lunar farside. MGM deconvolution on the in-situ measured spectra reveals materials at Chang'e-4 landing site have a Fo-rich OL and high-Mg OPX assemblage in almost equal fractions. The materials measured by the rover were actually a highly mixture of multiple sources, which were primarily the weathering products of Finsen crater ejecta. PLG, which has significant implication for the provenance of the measured materials, is often spectrally transparent or featureless in the wavelength range (450–2395 nm) of the in situ measured spectrum. Depending on the possible absence or presence of abundant PLG, the Chang'e-4 rover measured forsteritic OL and Mg-rich OPX materials likely originated from the differentiated SPA impact melt pool or from an Mg-suite pluton in the lunar lower crust, and were less likely to originate from the lunar upper mantle.

## Declaration of Competing Interest

The authors declare that they have no known competing financial interests or personal relationships that could have appeared to influence the work reported in this paper.

## Acknowledgments

The authors gratefully thank the whole Chang'e-4 team for making the mission a great success and for providing the data (<http://moon.bao.ac.cn>). This research is supported by the B-type Strategic Priority Program of the Chinese Academy of Sciences (grant No. XDB41000000), the National Natural Science Foundation of China (grant Nos. 41702354, 41941003, and 41972321), Macau Young Scholars Program (grant No. AM201902), and the Science and Technology Development Fund of Macau (grant No. 131/2017/A3). The authors greatly appreciated two anonymous reviewers for constructive comments that improved the manuscript quality substantially.

## Appendix A. Supplementary data

Supplementary data to this article can be found online at <https://doi.org/10.1016/j.icarus.2020.113776>.

## References

- Adams, J.B., 1974. Visible and near-infrared diffuse reflectance spectra of pyroxenes as applied to remote sensing of solid objects in the solar system. *J. Geophys. Res.* 79 (32), 4829–4836.
- Adams, J.B., Goullaud, L.H., 1978. Plagioclase feldspars-visible and near infrared diffuse reflectance spectra as applied to remote sensing. In: 9th Lunar and Planetary Science Conference, pp. 2901–2909.
- Adams, J.B., Horz, F., Gibbons, R.V., 1979. Effects of shock-loading on the reflectance spectra of plagioclase, pyroxene, and glass. In: 10th Lunar and Planetary Science Conference. Pergamon Press, Houston, TX, pp. 1–3.
- Barker, M.K., Mazarico, E., Neumann, G.A., Zuber, M.T., Haruyama, J., Smith, D.E., 2016. A new lunar digital elevation model from the lunar orbiter laser altimeter and SELENE terrain camera. *Icarus* 273, 346–355.
- Bruckenthal, E.A., Pieters, C.M., 1984. Spectral Effects of Natural Shock on Plagioclase Feldspar. 15th Lunar and Planetary Science Conference, Houston, TX, pp. 96–97.
- Burns, R.G., 1970. Crystal field spectra and evidence of cation ordering in olivine minerals. *Am. Mineral.* 55, 1608–1632.
- Burns, R.G., 1993. *Mineralogical Applications of Crystal Field Theory*, 2nd edition. Cambridge University Press, New York.

- Cannon, K.M., Mustard, J.F., 2015. Preserved glass-rich impactites on Mars. *Geology* 43 (7), 635–638.
- Cheek, L.C., Pieters, C.M., 2014. Reflectance spectroscopy of plagioclase-dominated mineral mixtures: implications for characterizing lunar anorthosites remotely. *Am. Mineral.* 99 (10), 1871–1892.
- Clénet, H., Pinet, P., Daydou, Y., Heuripeau, F., Rosemberg, C., Baratoux, D., Chevrel, S., 2011. A new systematic approach using the modified Gaussian model: insight for the characterization of chemical composition of olivines, pyroxenes and olivine–pyroxene mixtures. *Icarus* 213 (1), 404–422.
- Denevi, B.W., Lucey, P.G., Hochberg, E.J., Steutel, D., 2007. Near-infrared optical constants of pyroxene as a function of iron and calcium content. *J. Geophys. Res. Planets* 112 (E5), E05009.
- Ennis, M., Fagan, A., Pogue, J., Porter, S., Snape, J., 2012. Feasibility assessment of all science concepts within south pole-Aitken Basin. In: Kring, D.A., Durda, D.D. (Eds.), *A Global Lunar Landing Site Study to Provide the Scientific Context for Exploration of the Moon*. Lunar and Planetary Institute, Houston, pp. 477–562.
- Garrick-Bethell, I., Zuber, M.T., 2009. Elliptical structure of the lunar south pole-Aitken basin. *Icarus* 204 (2), 399–408.
- Gaul, O.F., Griffin, W.L., O'Reilly, S.Y., Pearson, N.J., 2000. Mapping olivine composition in the lithospheric mantle. *Earth Planet. Sci. Lett.* 182 (3), 223–235.
- He, Z., Li, C., Xu, R., Lv, G., Yuan, L., Wang, J., 2019. Spectrometers based on acousto-optic tunable filters for in-situ lunar surface measurement. *J. Appl. Remote. Sens.* 13 (2), 27502.
- Horgan, B.H.N., Cloutis, E.A., Mann, P., Bell, J.F., 2014. Near-infrared spectra of ferrous mineral mixtures and methods for their identification in planetary surface spectra. *Icarus* 234, 132–154.
- Huang, J., Xiao, Z., Flahaut, J., Martinot, M., Head, J., Xiao, X., Xie, M., Xiao, L., 2018. Geological characteristics of Von Kármán crater, northwestern south pole-Aitken Basin: Chang'E-4 landing site region. *J. Geophys. Res. Planets* 123 (7), 1684–1700.
- Hurwitz, D.M., Kring, D.A., 2014. Differentiation of the south pole-Aitken basin impact melt sheet: implications for lunar exploration. *J. Geophys. Res. Planets* 119 (6), 1110–1133.
- Isaacson, P.J., Pieters, C.M., 2010. Deconvolution of lunar olivine reflectance spectra: implications for remote compositional assessment. *Icarus* 210 (1), 8–13.
- Isaacson, P.J., Pieters, C.M., Besse, S., Clark, R.N., Head, J.W., Klima, R.L., Mustard, J.F., Petro, N.E., Staid, M.I., Sunshine, J.M., 2011. Remote compositional analysis of lunar olivine-rich lithologies with moon mineralogy mapper (M3) spectra. *J. Geophys. Res. Planets* 116 (E6), E00G11.
- Ivanov, M.A., Hiesinger, H., van der Bogert, C.H., Orgel, C., Pasckert, J.H., Head, J.W., 2018. Geologic history of the northern portion of the south pole-Aitken Basin on the moon. *J. Geophys. Res. Planets* 123 (10), 2585–2612.
- Jolliff, B., Alkalai, L., Pieters, C., Head, J., Papanastassiou, D., Bierhaus, E., 2010. Sampling the south pole-Aitken Basin: Objectives and site selection criteria. In: *41st Lunar and Planetary Science Conference*, p. 2450.
- Kanner, L.C., Mustard, J.F., Gendrin, A., 2007. Assessing the limits of the modified Gaussian model for remote spectroscopic studies of pyroxenes on Mars. *Icarus* 187 (2), 442–456.
- Li, C.L., Xu, R., Lv, G., Yuan, L.Y., He, Z.P., Wang, J.Y., 2019. Detection and calibration characteristics of the visible and near-infrared imaging spectrometer in the Chang'e-4. *Rev. Sci. Instrum.* 90 (10), 103106.
- Ling, Z., Jolliff, B.L., Liu, C.Q., Bi, X.Y., Liu, L., Qiao, L., Zhang, J., Fu, X., Liu, J., 2018. Composition, mineralogy, and chronology of Mare basalts in Von Kármán crater: A candidate landing site of Chang'e-4. In: *49th Lunar and Planetary Science Conference*, the Woodlands, Texas, p. 1939.
- Liu, B., Niu, S., Xin, X., Jia, M., Di, K., Liu, Z., Peng, M., Yue, Z., 2019. High precision DTM and DOM generating using multi-source orbital data on Chang'e-4 landing site. In: *Int. Arch. Photogramm. Remote Sens. Spatial Inf. Sci.*, XLII-2/W13. Copernicus Publications, Enschede, The Netherlands, pp. 1413–1417.
- Melosh, H.J., Kendall, J., Horgan, B., Johnson, B.C., Bowling, T., Lucey, P.G., Taylor, G. J., 2017. South pole-Aitken basin ejecta reveal the Moon's upper mantle. *Geology* 45 (12), 1063–1066.
- Miljkovic, K., Wieczorek, M.A., Collins, G., C. Solomon, S., E. Smith, D., T. Zuber, M., 2015. Excavation of the mantle in basin-forming events on the moon. *Earth Planet. Sci. Lett.* 409, 243–251.
- Moriarty, D.P., Pieters, C.M., 2016. Complexities in pyroxene compositions derived from absorption band centers: examples from Apollo samples, HED meteorites, synthetic pure pyroxenes, and remote sensing data. *Meteorit. Planet. Sci.* 51 (2), 207–234.
- NRC, 2011. *Vision and Voyages for Planetary Science in the Decade 2013–2022*. National Research Council, Washington, D.C.
- Otake, H., Ohtake, M., Hirata, N., 2012. Lunar Iron and titanium abundance algorithms based on SELENE (Kaguya) multiband imager data. In: *43rd Lunar and Planetary Science Conference*, the Woodlands, Texas, p. 1905.
- Papike, J.J., Hodges, F.N., Bence, A.E., Cameron, M., Rhodes, J.M., 1976. Mare basalts: crystal chemistry, mineralogy, and petrology. *Rev. Geophys.* 14 (4), 475–540.
- Petro, N.E., 2011. Volume of impact melt generated by the formation of the south pole-Aitken Basin. In: *Annual Meeting of the Lunar Exploration Analysis Group*, Houston, Texas, p. 2051.
- Petro, N.E., Pieters, C.M., 2002. The size and location of the transient crater of the south pole-Aitken Basin. In: *33rd Lunar and Planetary Science Conference*, Houston, Texas, p. 1848.
- Pieters, C.M., 1986. Composition of the lunar highland crust from near-infrared spectroscopy. *Rev. Geophys.* 24 (3), 557–578.
- Pieters, C.M., Noble, S.K., 2016. Space weathering on airless bodies. *J. Geophys. Res. Planets* 121 (10), 1865–1884.
- Pinet, P., 2019. The Moon's mantle unveiled. *Nature*. *Nature* 569, 338–339.
- Pinet, P.C., Chevrel, S.D., Daydou, Y.H., 2018. Characterization of the olivine/plagioclase mineralogy at Copernicus crater from MGM Deconvolution of M3 observations. In: *49th Lunar and Planetary Science Conference*, the Woodlands, Texas.
- Pinet, P.C., Chevrel, S.D., Daydou, Y.H., 2019. Reassessing the relationship between olivine composition and reflectance spectroscopy from advanced MGM deconvolution. In: *50th Lunar and Planetary Science Conference*, the Woodlands, Texas.
- Potter, R.W.K., Collins, G.S., Kiefer, W.S., McGovern, P.J., Kring, D.A., 2012. Constraining the size of the south pole-Aitken basin impact. *Icarus* 220 (2), 730–743.
- Ringwood, A.E., Kesson, S.E., 1976. A dynamic model for mare basalt petrogenesis. In: *7th Lunar Science Conference*. Pergamon Press, Houston, Texas, pp. 1697–1722.
- Robinson, M.S., Brylow, S.M., Tschimmel, M., Humm, D., Lawrence, S.J., Thomas, P.C., Denevi, B.W., Bowman-Cisneros, E., Zerr, J., Ravine, M.A., Caplinger, M.A., Ghaemi, F.T., Schaffner, J.A., Malin, M.C., Mahanti, P., Bartels, A., Anderson, J., Tran, T.N., Eliason, E.M., McEwen, A.S., Turtle, E., Jolliff, B.L., Hiesinger, H., 2010. Lunar reconnaissance orbiter camera (LROC) instrument overview. *Space Sci. Rev.* 150 (1–4), 81–124.
- Schultz, P.H., Crawford, D.A., 2011. Origin of nearside structural and geochemical anomalies on the moon. *Geol. Soc. Am. Spec. Pap.* 477, 141–159.
- Shearer, C.K., Burger, P.V., Bell, A.S., Guan, Y., Neal, C.R., 2015. Exploring the Moon's surface for remnants of the lunar mantle 1. Dunitic xenoliths in mare basalts. A crustal or mantle origin? *Meteorit. Planet. Sci.* 50 (8), 1449–1467.
- Smith, D.E., Zuber, M.T., Neumann, G.A., Lemoine, F.G., Mazarico, E., Torrence, M.H., McGarry, J.F., Rowlands, D.D., Head III, J.W., Duxbury, T.H., Aharonson, O., Lucey, P.G., Robinson, M.S., Barnouin, O.S., Cavanaugh, J.F., Sun, X., Liiva, P., Mao, D.-d., Smith, J.C., Bartels, A.E., 2010. Initial observations from the lunar orbiter laser altimeter (LOLA). *Geophys. Res. Lett.* 37 (18), L18204.
- Spudis, P.D., Davis, P.A., 1986. A chemical and petrological model of the lunar crust and implications for lunar crustal origin. *J. Geophys. Res. Solid Earth* 91 (B13), E84–E90.
- Spudis, P.D., Gillis, J.J., Reisse, R.A., 1994. Ancient multiring basins on the moon revealed by Clementine laser altimetry. *Science* 266 (5192), 1848–1851.
- Stuart-Alexander, D.E., 1978. Geologic map of the central far side of the moon IMAP 1047.** <http://pubs.er.usgs.gov/publication/i1047>.
- Sunshine, J.M., Pieters, C.M., 1998. Determining the composition of olivine from reflectance spectroscopy. *J. Geophys. Res.* 103 (E6), 13675–13688.
- Sunshine, J.M., Pieters, C.M., Pratt, S.F., 1990. Deconvolution of mineral absorption bands - an improved approach. *J. Geophys. Res.* 95 (B5), 6955–6966.
- Vaughan, W.M., Head, J.W., 2014. Impact melt differentiation in the south pole-Aitken basin: some observations and speculations. *Planet. Space Sci.* 91, 101–106.
- Wieczorek, M.A., Phillips, R.J., 1999. Lunar multiring basins and the cratering process. *Icarus* 139 (2), 246–259.
- Wilhelms, D.E., Howard, K.A., Wilshire, H.G., 1979. Geologic map of the south side of the moon. In: *U.S.G.S. Misc. Inves. Ser. Map I-1162, 1:5M Scale*.
- Wu, Y., Wang, Z., Cai, W., Lu, Y., 2018. The absolute reflectance and new calibration site of the moon. *Astron. J.* 155 (5), 213.
- Wu, W., Li, C., Zuo, W., Zhang, H., Liu, J., Wen, W., Su, Y., Ren, X., Yan, J., Yu, D., Dong, G., Wang, C., Sun, Z., Liu, E., Yang, J., Ouyang, Z., 2019. Lunar farside to be explored by Chang'e-4. *Nat. Geosci.* 12 (4), 222–223.
- Yamamoto, S., Nakamura, R., Matsunaga, T., Ogawa, Y., Ishihara, Y., Morota, T., Hirata, N., Ohtake, M., Hiroi, T., Yokota, Y., Haruyama, J., 2010. Possible mantle origin of olivine around lunar impact basins detected by SELENE. *Nat. Geosci.* 3, 533–536.
- Zhu, M.-H., Wünnemann, K., Morbidelli, A., Artemieva, N.A., 2018. South pole-Aitken basin may contribute insignificantly to the late accretion of the moon. In: *49th Lunar and Planetary Science Conference*, the Woodlands, Texas, p. 1955.